

EXPERIMENTAL INVESTIGATIONS ON VORTEX FLOW PHENOMENA OF A DIAMOND WING CONFIGURATION

Andreas Hövelmann* , Christian Breitsamter*

*Institute of Aerodynamics and Fluid Mechanics, Technische Universität München

Andreas.Hoevermann@tum.de, Christian.Breitsamter@aer.mw.tum.de

Keywords: Applied Aerodynamics, Experimental Aerodynamics, Diamond Wing, UAV, Vortex Flow

Abstract

A 55° leading-edge sweep diamond wing configuration named SAGITTA is studied experimentally at low speed conditions with different measurement techniques. Wind tunnel results of aerodynamic forces and moments and steady surface pressure measurements as well as flow field characteristics gathered from Stereo Particle Image Velocimetry are presented. Because of span-wise varying leading-edge contours, different regions of separated flow occur on the diamond wing configuration with increasing angle of attack. Due to the 12% relative thickness airfoil, vortex formation only takes place at the sharp inboard leading-edge segment. In the wing tip area, in contrast, where rounded leading-edge contours are present, the emerging separation region is dominated by irregular flow with flow reversal. For the angle of attack of $\alpha = 16^\circ$, the resulting flow field is discussed in detail with regard to overall aerodynamic characteristics, mean velocity distributions and turbulent flow field quantities. The trajectory of the inboard vortex and the structure of the wing tip separation area are thereby analyzed.

Nomenclature

b	Wing Span, [m]
C_D	Drag Coefficient, $C_D = \frac{D}{q_\infty \cdot S_{Ref}}$
C_L	Lift Coefficient, $C_L = \frac{L}{q_\infty \cdot S_{Ref}}$
C_m	Pitching Moment Coefficient, $C_m = \frac{m}{q_\infty \cdot S_{Ref} \cdot l_\mu}$
c	Wing Chord, [m]

c_p	Pressure Coefficient, $c_p = \frac{p-p_\infty}{q_\infty}$
D	Drag, [N]
d	Diameter, [m]
E	Power, [J]
F	Focal Length, [m]
f	Frequency, [Hz]
k	Non-Dimensional Turbulent Kinetic Energy
L	Lift, [N]
l_μ	Mean Aerodynamic Chord, [m]
Ma	Mach Number
m	Pitching Moment, [Nm]
p	Static Pressure, [N/m ²]
p_∞	Freestream Static Pressure, [N/m ²]
q_∞	Freestream Dynamic Pressure, [N/m ²]
Re	Reynolds Number
r_N	Leading-Edge Radius, [m]
S_{Ref}	Wing Reference Area, [m ²]
s	Wing Half Span, [m]
t	Time, [s]
U_∞	Freestream Velocity, [m/s]
u, v, w	Velocity Components, [m/s]
u', v', w'	Fluctuation Part of u, v, w , [m/s]
x, y, z	Cartesian Coordinates, [m]
α	Angle of Attack, [deg]
Λ	Wing Aspect Ratio
λ	Wing Taper Ratio
φ	Wing Sweep Angle, [deg]
ψ	Wave Length, [m]
ω_x	Axial Vorticity, [1/s]

Subscripts

LE	Leading-Edge
Max	Maximum Value
MRP	Moment Reference Point
mean	Time-Averaged Mean Value

meas	Measurement
r	Root Chord
rms	Root Mean Square
TE	Trailing-Edge
t	Tip Chord

1 Introduction

While vortex flow phenomena at thin and slender delta wing configurations ($\phi_{LE} \geq 60^\circ$) with sharp leading-edges have been studied for many years, the effects of changed influence parameters on leading-edge vortex characteristics such as reduced wing sweep (non-slender configurations with $50^\circ \leq \phi_{LE} \leq 55^\circ$) or rounded leading-edges are still under investigation in research [1, 2]. Moreover, modified geometry planforms (lambda and diamond wings), span-wise varying leading-edge contours (sharp and rounded) and much thicker airfoils are currently considered for vortex flow analyses [3, 4]. These types of investigations are mainly motivated by today's developments of typical low signature low aspect ratio wing configurations, which often focus on unmanned aerial vehicles (UAV).

In this context, the Institute of Aerodynamics and Fluid Mechanics of Technische Universität München (TUM-AER) investigates the aerodynamic characteristics of the SAGITTA diamond wing configuration. Special attention is thereby put on the occurring vortex flow phenomena. The SAGITTA diamond wing configuration refers to a research program of Airbus Defence & Space, in which a so called Open Innovation approach is followed [5]. Overall, the investigations are performed both numerically and experimentally. On the one hand, numerous CFD computations are undertaken. Thereby, the flow field around the SAGITTA diamond wing configuration is analyzed and the main aerodynamic characteristics have already been published [3]. On the other hand, a wind tunnel (W/T) model has been built, on which the experimental analyses are performed, Section 2.1.

In the present publication, experimental results gained from W/T tests on the SAGITTA diamond wing configuration are presented. The focus of the paper is laid on the measurement tech-

niques applied and the detailed analysis of the experimental results. At first, the overall aerodynamic characteristics are regarded. Afterwards, both the mean and the turbulent flow field characteristics are addressed. The vortex flow phenomena and other flow separation structures occurring are thus discussed.

2 Experimental Approach

2.1 The SAGITTA Diamond Wing Wind Tunnel Configuration

The manufactured W/T model represents the SAGITTA diamond wing wind tunnel configuration. Featuring a root chord length of $c_r = 1.2\text{ m}$, it is a 1:10-scaled version of the original SAGITTA diamond wing configuration, which stands for the overall reference geometry within the SAGITTA research analyses [5]. The corresponding diamond wing planform of the W/T model is presented in Figure 1, while Table 1 summarizes the main planform parameters.

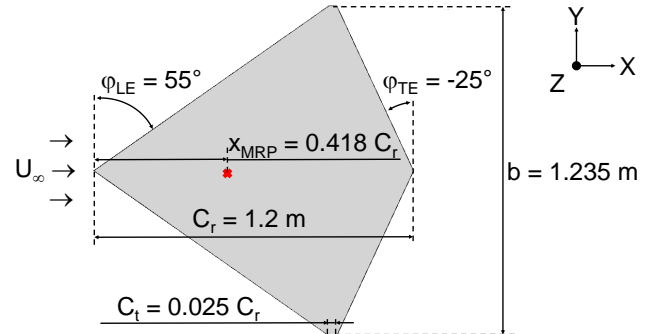


Fig. 1 SAGITTA diamond wing W/T configuration, top view xy plane.

c_r	c_t	λ	ϕ_{LE}	ϕ_{TE}
[m]	[m]	[-]	[°]	[°]
1.2	0.03	0.025	55	-25
b	S_{Ref}	Λ	l_μ	x_{MRP}
[m]	[m ²]	[-]	[m]	[m]
1.235	0.760	2.001	0.801	0.502

Table 1 Wing planform parameters of the SAGITTA diamond wing W/T configuration.

The UAV configuration of 55° leading-edge sweep features a symmetric airfoil of 12% relative thickness (NACA64A012), which results in a relatively large nose radius of the rounded leading-edge ($r_N/c = 0.994\%$). At the inner 20% of the wing half span, however, the rounded leading-edge shape is replaced by a sharp leading-edge contour to stimulate vortex formation. In the following, this configuration is referred to as SG-RS_Mod-00. Former studies on this 12% relative thickness UAV have shown that even at moderate to higher angles of attack, wing segments with rounded leading-edge contours are dominated by attached flow (apart from the tapered wing tip area). Vortex formation only takes place with sharp leading-edge contours [3, 6].

The corresponding W/T model is built as aluminium full model out of Certal, Figure 2. It allows for the study of different leading-edge contours, as the model features exchangeable leading-edge segments. Thereby, leading-edge geometry modifications can be treated such as it has been analyzed previously via CFD [3]. So far, however, the leading-edge contour of the reference configuration SG-RS_Mod-00 is available exclusively for the W/T model.



Fig. 2 SAGITTA diamond wing W/T configuration within the test section.

2.2 Wind Tunnel Test Facility and Test Conditions

The experiments are carried out in the W/T facility A of TUM-AER. The Göttingen-type low speed tunnel has an open test section with the

dimensions of 1.8 m x 2.4 m x 4.8 m (height x width x length). The maximum velocity usable for experiments with the open test section is $U_{\infty,Max} = 65 \text{ m/s}$ and the freestream turbulence intensity reads 0.4%. The uncertainty in the temporal and spatial mean velocity distribution is less than 0.7%. The uncertainty in freestream direction is below 0.2° and static pressure variations are below 0.4%.

A three-axis model support is used to mount the W/T model with a rear sting in the test section, Figure 2. For the present analysis, however, the longitudinal motion is regarded exclusively, for which the angle of attack is adjusted computer-controlled during the W/T experiments. Overall, aerodynamic force and moment and steady surface pressure measurements are conducted for angles of attack of $-4^\circ \leq \alpha \leq 20^\circ$. Flow field measurements with Stereo Particle Image Velocimetry are undertaken for three angles of attack ($\alpha = 12^\circ$, $\alpha = 16^\circ$, and $\alpha = 24^\circ$).

The freestream conditions are characterized by a Mach number of $Ma = 0.13$ and a Reynolds number of $Re = 2.3 \cdot 10^6$ based on the mean aerodynamic chord of $l_\mu = 0.801 \text{ m}$. In order to assure turbulent boundary layer characteristics on the entire W/T model, aeronautical trip dots are attached close to the leading-edge. Doing so, the transition is fixed at the W/T model and fully turbulent CFD computations are relevant for comparison of numerical and experimental data.

2.3 Measurement Techniques

2.3.1 Force Measurements

The aerodynamic coefficients are obtained with an internal six component strain gauge balance, which measures the forces and moments acting on the W/T model. The maximum allowed loads are 900 N, 450 N, and 2500 N for axial, lateral and normal forces, respectively. The maximum sustainable moments read 120 Nm, 160 Nm, and 120 Nm for rolling, pitching, and yawing moments, respectively [7].

For data acquisition, a measurement time of $t_{meas} = 20 \text{ s}$ is chosen with a sampling rate of $f_{meas} = 1200 \text{ Hz}$. The results of the aerodynamic coefficients presented here are, however, time-

averaged values. Furthermore, repeatability tests over eight polar runs show for the present test setup deviances in the longitudinal aerodynamic coefficients of $\Delta C_{D,Max} = \pm 0.0011$, $\Delta C_{L,Max} = \pm 0.0028$ and $\Delta C_{m,Max} = \pm 0.0003$.

2.3.2 Steady Surface Pressure Measurements

Overall, 192 pressure tabs are available on the W/T model that are used for steady surface pressure measurements. Every orifice is aligned normal to the wing surface and features a diameter of $d = 0.3 \text{ mm}$. 160 pressure tabs are located on the suction side of the right wing half in seven different chord-wise sections ($x/c_r = 0.1$ to $x/c_r = 0.7$ with $\Delta x/c_r = 0.1$). Approaching the leading-edge of each section along the wing half span, the spacing of the pressure tabs becomes closer to get more pressure information in the regions of interest. In order to study symmetry concerns with respect to the xy - and the xz - plane, 32 additional pressure tabs are located on the pressure side of the right wing half and the suction side of the left wing half.

The steady surface pressure measurements are conducted with three electronic pressure scanning modules, which are located within the W/T model. An averaging time of $t_{meas} = 10 \text{ s}$ and a sampling rate of $f_{meas} = 200 \text{ Hz}$ is applied to measure and process the pressure tab signals. The data sets shown in the present analysis always refer to mean values $c_{p,mean}$. Due to repeatability tests performed for the surface pressure measurements, the measurement accuracy reads $\Delta c_{p,mean,Max} = \pm 0.013$. This value represents the averaged deviance over all pressure tabs and all considered angles of attack.

2.3.3 Stereo Particle Image Velocimetry

For the generation of flow field data sets in different chord-wise sections, the Stereo Particle Image Velocimetry (Stereo PIV) is applied. The overall setup of the measurement technique in the W/T facility A of TUM-AER is shown in Figure 2 and Figure 3. All relevant components are placed on a three-axis traversing system, which is located next to the W/T test section.

For the laser sheet formation, a double-pulse

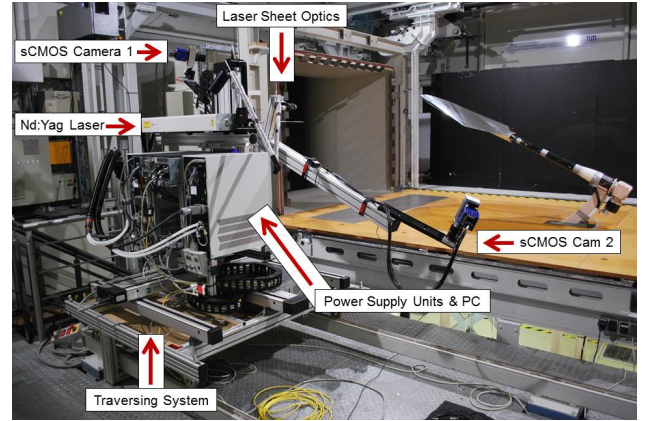


Fig. 3 Stereo PIV system in the W/T facility A of TUM-AER.

Nd:Yag laser with a maximum power of $E = 325 \text{ mJ}$ is used. The associated wave length reads $\psi = 532 \text{ nm}$, appearing in visible green light. The measurement field of view is defined by a laser sheet optic (cylindrical lens), which converts the laser beam to a sheet and aligns the resulting laser sheet normal to the chord line of the diamond wing surface. Up- and downstream of the laser sheet optic, two high-speed sCMOS cameras with a resolution of 2560×2160 pixels are placed, Figure 3. In the present measurement setup, NIKON objective lenses with a focal length of $F = 135 \text{ mm}$ are used. The application of two cameras allows for the simultaneous measurement of all three velocity components in the measurement field of view (Stereo PIV). Furthermore, Scheimpflug adapters are mounted between the sCMOS sensor plane and the lens to account for tilting the sCMOS sensor plane with respect to the off-axis camera [8]. In order to minimize reflections of the laser sheet on the W/T model seen by the cameras, the relative position of the up- and downstream cameras and the laser sheet optic is aligned with the angle of attack of the W/T model, Figure 4. This has been the outcome of comparable former studies dealing with Stereo PIV measurements of swept wing configurations [9, 10, 11, 12] and numerous tests conducted in preparation of this experimental campaign. Moreover, the model does not have to be coated in the present W/T setup for minimizing reflections. The flow field measurements are still possible down to the diamond wing surface.

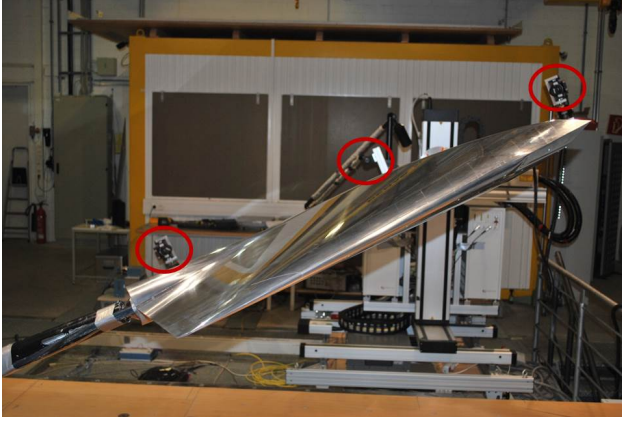


Fig. 4 Position of laser sheet optic and sCMOS cameras in relation to the W/T model.

For the Stereo PIV measurements, seeding particles are intermixed with the air in the W/T test section. At two instants ($\Delta t = 12$ ns in the present W/T test), the double-pulse laser illuminates the shaded W/T facility and the high-speed sCMOS cameras record two raw images each. Based on the relative movement of the particles between the two instants and a proper calibration of the entire optical setup, the velocity components are calculated by mathematical and statistical methods [8]. For one W/T run and per measurement slice, 400 sequences are recorded each with a sampling frequency of $f_{meas} = 12$ Hz. Over these data sets, the results are averaged, which finally results in mean and turbulent velocity flow fields. The underlying evaluation parameters and main information about the resulting vector fields are summarized in Table 2. Due to constraints of the global Stereo PIV setup, the chord-wise sections measured start at $x/c_r = 0.2$ and extend to $x/c_r = 0.7$ with an interval of $\Delta x/c_r = 0.05$.

3 Results and Discussion

In this section, the experimental results performed on the SAGITTA diamond wing W/T configuration are presented and discussed mainly for one specific angle of attack, namely $\alpha = 16^\circ$. At first, Section 3.1 introduces the overall aerodynamic characteristics of the present diamond wing. Then, Section 3.2 and Section 3.3 depict the mean and the turbulent velocity field in detail for different chord-wise sections at $\alpha = 16^\circ$.

Main algorithm	Stereo cross-correlation with image deformation
Iteration options	Multi-pass, decreasing size, 4 passes
Size of final interrogation window	32 x 32 pixel
Overlapping	0%
Final field of view	600 mm x 155 mm
Number of vectors	≈ 6500
Spatial resolution	3.7 mm x 3.7 mm

Table 2 Stereo PIV evaluation parameters.

3.1 Overall Aerodynamic Characteristics

3.1.1 Flow Field

With increasing angle of attack, the flow field of the diamond wing configuration is particularly distinguished by two main flow phenomena. In order to clarify them, Figure 5 shows the axial vorticity component $\omega_{x,mean} \cdot l_\mu / U_\infty$ at $\alpha = 16^\circ$.

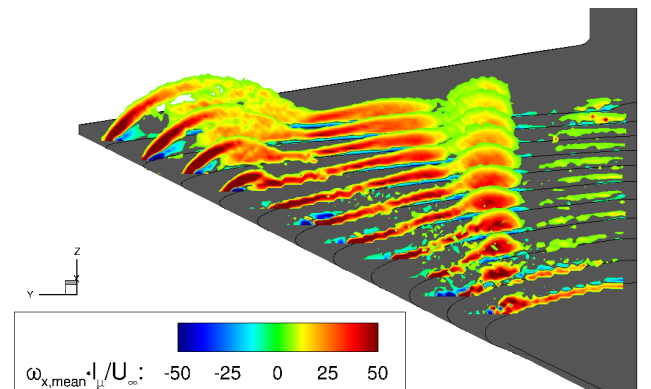


Fig. 5 Axial vorticity component $\omega_{x,mean} \cdot l_\mu / U_\infty$ at $\alpha = 16^\circ$.

Due to the sharp inboard leading-edge contour as introduced in Section 2.1, a distinct leading-edge vortex is formed in the inboard section of the diamond wing. At the first Stereo PIV slice shown in Figure 5 ($x/c_r = 0.2$), the leading-edge contour has already changed to the rounded NACA airfoil, which is then kept constant in span-wise direction up to the diamond wing tip. High axial vorticity levels are observed close to the leading-edge, but the vortex starts to deviate from it. In downstream direction, the inboard vortex

does not follow the leading-edge anymore, but the trajectory is aligned with the main flow in chord-wise direction. Up to the most downstream chord-wise section at $x/c_r = 0.7$, the inboard leading-edge vortex is detected. Moving downstream, the intensity characterized by the maximum contour levels of the axial vorticity slightly decreases.

The corresponding axial velocities u_{mean}/U_∞ in the vicinity of the inboard leading-edge vortex are displayed in Figure 6. It can be noticed that the axial flow transport with respect to the freestream velocity is slightly retarded within the vortex core. In contrast to typical slender and thin delta wings with sharp leading-edge contours, for which the axial velocity components of the vortex core are increased up to $u_{mean}/U_\infty \approx 2 - 5$ [13], the present observation is typical for this type of non-slender diamond wing including a thick airfoil.

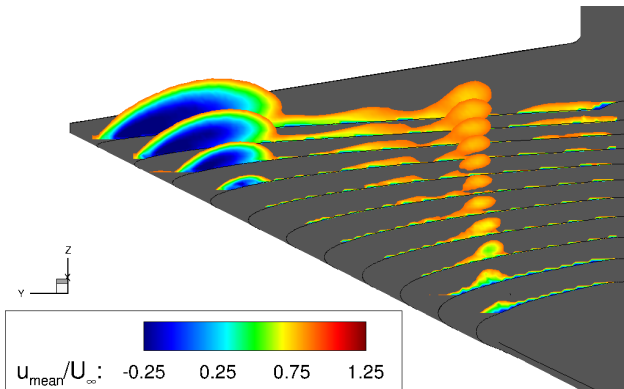


Fig. 6 Axial velocity component u_{mean}/U_∞ at $\alpha = 16^\circ$.

The second flow phenomenon is the flow separation emerging in the diamond wing tip region, which occurs due to the drastically reduced chord length. For the present angle of attack of $\alpha = 16^\circ$, the area of separated flow extends from the chord-wise section at $x/c_r = 0.55$ to the trailing-edge. Close to the rounded leading-edge contour, high levels of the axial vorticity component $\omega_{x,mean}$ are noticed at the separating shear layer, Figure 5. A distinct vortex structure, however, is not formed, but a recirculation area, Figure 6. Within the area of separated flow, the axial velocity component becomes negative, which

proves the evidence of flow reversal. Thereby, no stable leading-edge vortex with positive axial fluid transport is built, but a region of irregular flow.

3.1.2 Surface Flow

Figure 7 depicts the corresponding surface flow characteristics at $\alpha = 16^\circ$, gathered from the steady surface pressure measurements in different chord-wise sections. The inboard leading-edge vortex is clearly observed up to the chord-wise section at $x/c_r = 0.4$ by pronounced suction peaks. More downstream, the suction levels are close to them of the adjacencies, which confirms the decreasing intensity of the inboard leading-edge vortex over the diamond wing surface.

The wing tip separation region, in contrast, can not be detected with the present layout of

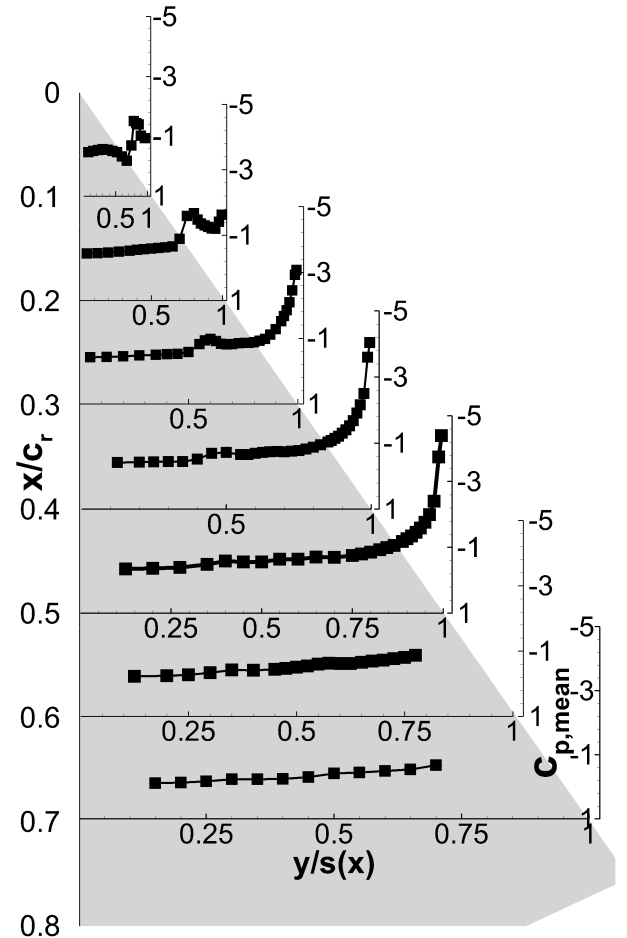


Fig. 7 Surface pressure coefficient $c_{p,mean}$ versus non-dimensional half span $y/s(x)$ at $\alpha = 16^\circ$.

the pressure tabs. Due to space and construction restrictions of the W/T model, the measurement slices at $x/c_r \geq 0.6$ do not contain pressure tabs close to the leading-edge.

Upstream of the emerging flow separation region, leading-edge suction peaks are observed in the chord-wise sections at $0.3 \leq x/c_r \leq 0.5$, Figure 7. In this region, the W/T model exhibits a rounded leading-edge contour. Consequently, attached flow is present in the midboard sections of the SAGITTA diamond wing W/T configuration, even at the angle of attack of $\alpha = 16^\circ$. Due to the non-slender wing planform and the large leading-edge radius of the airfoil of 12% relative thickness, as introduced in Section 2.1, vortex formation does not take place for the rounded leading-edge contour.

3.1.3 Longitudinal Aerodynamic Coefficients

In the following, the integral values of the longitudinal aerodynamic coefficients are presented, Figure 8. Thereby, the overall aerodynamic characteristics of the SAGITTA diamond wing W/T configuration (SG-RS_Mod-00) are charac-

terized over the entire angle of attack range considered within the W/T investigations. At first, the lift coefficient C_L is regarded, which is shown in the left plot of Figure 8(a). Over the whole polar, an almost pure linear dependency is found. Despite the existence of the inboard leading-edge vortex, no distinct non-linear lift increase is observed for angles of attack of $10^\circ \leq \alpha \leq 20^\circ$. Furthermore, the maximum lift coefficient $C_{L,max}$ is not reached up to $\alpha = 20^\circ$. Due to occurring vibrations at the W/T model for the applied freestream velocity of $U_\infty \approx 47 \text{ m/s}$ ($Ma = 0.13$), the angle of attack is limited in the present analysis to $\alpha = 20^\circ$.

The corresponding plot of the pitching moment coefficient C_m is displayed on the right hand side of Figure 8(a). In contrast to the lift coefficient curve, the derivative dC_m/dC_L associated with the pitching moment coefficient curve is not constant anymore, but increases with increasing lift coefficient in its absolute value. The flow physics for this effect occurring with increasing angle of attack is dominated by the lift increase in the midboard sections, where attached flow

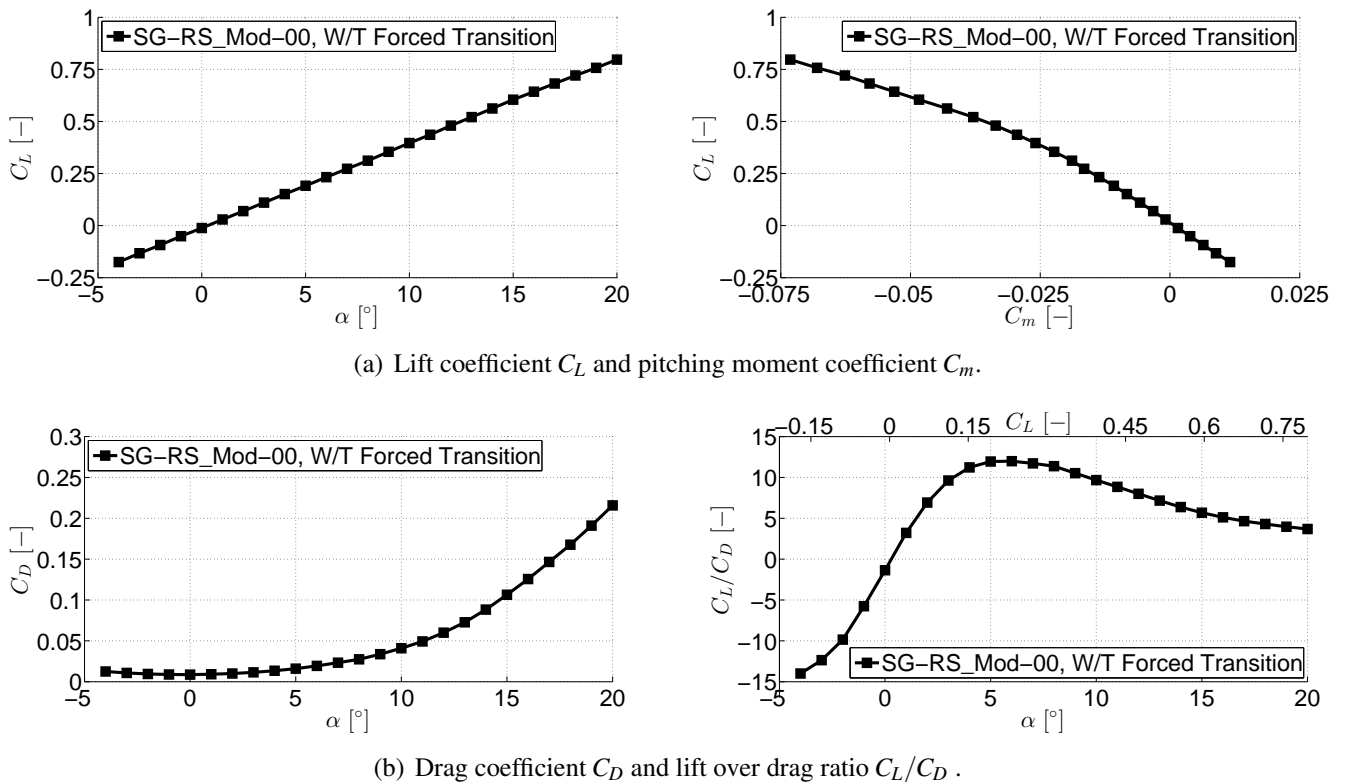


Fig. 8 Longitudinal aerodynamic coefficients C_D , C_L and C_m versus angle of attack α .

is present, Figure 7. The resulting local center of pressure of the midboard sections is located downstream of the moment reference point, leading to a nose down moment of the diamond wing. The other two flow phenomena, namely the increasing suction levels of the inboard leading-edge vortex in the more upstream sections and the loss of lift due to the outboard separation region, in contrast, arise a nose up moment with increasing angle of attack. These destabilizing effects, however, are outbalanced by the increasing lift of the attached flow in the midboard sections. Consequently, the stabilizing effect dominates the pitching moment characteristics with increasing angle of attack.

Next, the drag coefficient C_D is considered. The left plot of Figure 8(b) depicts the drag polar. The zero drag coefficient results in a value of $C_{D,0} = 0.0087$. Beyond that, the typical quadratic characteristic of the drag coefficient curve is observed. With increasing angle of attack, both lift induced drag as well as drag originating from the wing tip separation and the inboard leading-edge vortex are generated and lead to increased drag coefficient values.

Finally, the lift to drag ratio C_L/C_D is shown on the right hand side of Figure 8(b). The maximum of the curve is found at an angle of attack of $\alpha = 6^\circ$, for which the lift to drag ratio results in $(C_L/C_D)_{max} = 11.99$. At zero angle of attack, a small negative ratio is observed, although the SAGITTA diamond wing configuration is symmetrical with respect to the xy plane. This result derives from the slightly negative measured zero lift coefficient within the W/T investigations, which reads $C_{L,0} = -0.0118$.

3.2 Mean Flow Field Characteristics

In analogy to Figure 5, the axial vorticity component $\omega_{x,mean} \cdot l_\mu / U_\infty$ is presented in Figure 9 again for $\alpha = 16^\circ$, but now as two dimensional contour plot for three selected chord-wise sections. The occurring flow field characteristics become thereby more obvious. Overall, the results confirm the reasonable application of the Stereo PIV measurement technique, as the flow phenomena are captured down to the diamond wing surface.

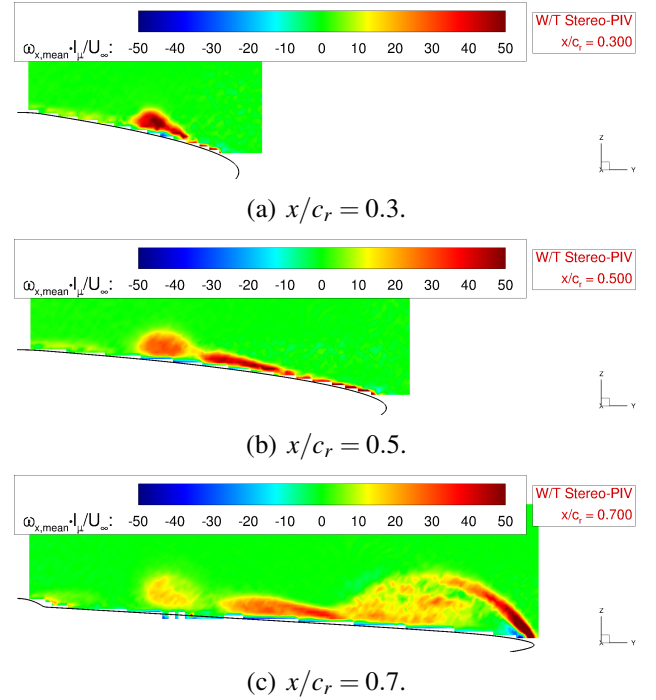


Fig. 9 Axial vorticity component $\omega_{x,mean} \cdot l_\mu / U_\infty$ for selected chord-wise sections at $\alpha = 16^\circ$.

By example, Figure 9(b) and Figure 9(c) display in addition to the inboard vortex and the wing tip separation also the thickened boundary layer in between. It is formed in the more downstream region of the midboard wing sections due to the other two structures of separated flow. Furthermore, the separating shear layer at the leading-edge of the wing tip region is captured well, showing very high axial vorticity levels, Figure 9(c). A roll-up mechanism to a defined vortex structure, however, is not observed. In contrast, a diffuse distribution of increased axial vorticity levels is present within the wing tip separation area.

Figure 10 depicts the axial velocity component u_{mean}/U_∞ , and surface streamlines are added to the contour plot for three different chord-wise sections. At $x/c_r = 0.3$, the inboard vortex with the retarded axial velocity in the vortex core is observed, Figure 10(a). The corresponding streamlines precisely indicate the vortex axis. More downstream at the chord-wise position of $x/c_r = 0.5$, the inboard vortex structure has grown in size, Figure 10(b). The streamline patterns show that the fluid transport is exclu-

Experimental Investigations on Vortex Flow Phenomena of a Diamond Wing Configuration

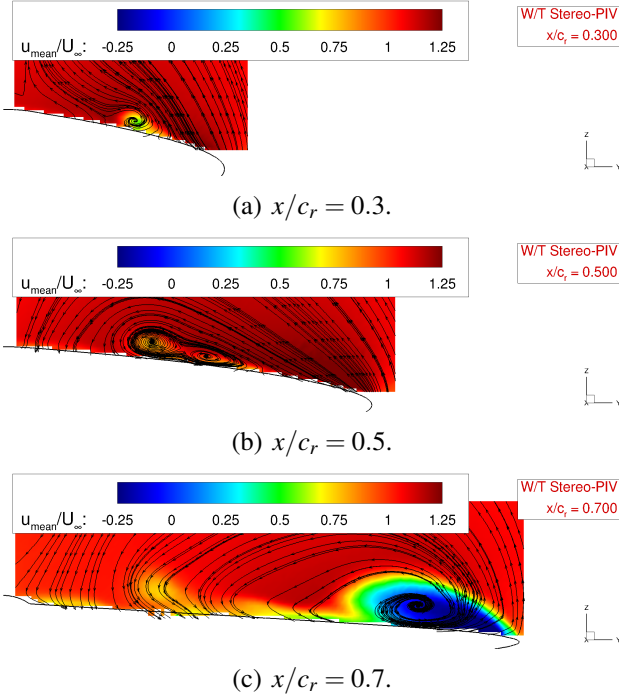


Fig. 10 Axial velocity component u_{mean}/U_{∞} for selected chord-wise sections at $\alpha = 16^{\circ}$.

sively directed downstream. Next to the inboard vortex, a second rotating structure is furthermore identified. It can be assigned to the thickened boundary layer region introduced above. It becomes obvious that this region starts to merge into a further region of irregular flow, forming a separation bubble. Between the two structures discussed, the separation line of the inboard vortex is located. In the most downstream chord-wise section at $x/c_r = 0.7$, shown in Figure 9(c), the streamline patterns are now dominated by the wing tip separation. The streamline characteristics clearly show the leading-edge separation and the occurring flow reversal within the wing tip separation area. Further inboard, the velocity deficit of the inboard leading-edge vortex and the thickened boundary layer region is observed. Moreover, the streamline patterns of this region are also influenced by the wing tip separation.

The other two velocity components, v_{mean}/U_{∞} and w_{mean}/U_{∞} , are regarded in Figure 11 and Figure 12. In addition to the contour levels, cross flow velocity vectors are displayed in the corresponding plots. Considering the lateral velocity component, the displacement of the inboard vor-

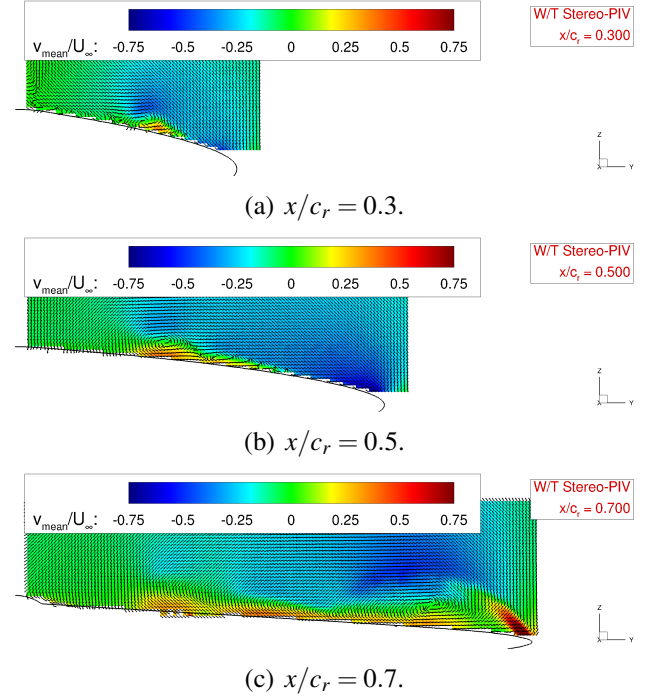


Fig. 11 Lateral velocity component v_{mean}/U_{∞} for selected chord-wise sections at $\alpha = 16^{\circ}$.

tex axis from the wing surface can be analyzed, Figure 11. It is characterized by the zero-crossing and the change of sign of v_{mean}/U_{∞} . Especially at the chord-wise position of $x/c_r = 0.5$, it can be observed very well, Figure 11(b).

As it can be expected, high negative values of the lateral velocity component are noticed above the inboard vortex axis and in the vicinity of the leading-edge with attached flow, Figure 11(a) and Figure 11(b). At $x/c_r = 0.7$, in contrast, where the wing tip separation occurs, large positive values of v_{mean}/U_{∞} are locally found close to the leading-edge, Figure 11(c). It seems obvious that due to the flow separation, the negative components of the lateral velocity decrease close to the leading-edge, but the intensity of the outboard directed lateral velocity measured within the W/T investigations is noticeable.

Finally, the velocity distribution of the normal component w_{mean}/U_{∞} is discussed, Figure 12. The most noticeable variations of w_{mean}/U_{∞} in the mean velocity field appear for all three chord-wise sections considered in the vicinity of the leading-edge. In general, the circulation leads to positive values of the normal velocity compo-

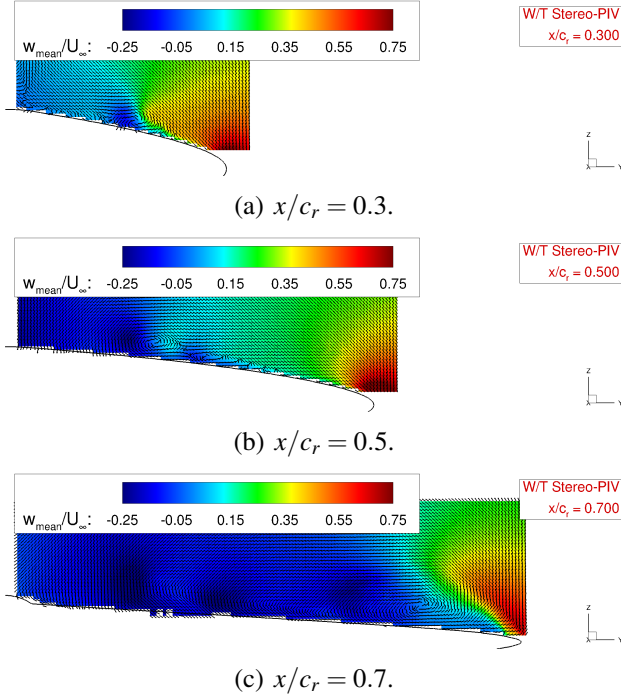


Fig. 12 Normal velocity component w_{mean}/U_∞ for selected chord-wise sections at $\alpha = 16^\circ$.

nents close to the leading-edge. At the chord-wise position of $x/c_r = 0.7$, the wing tip separation induces additional positive normal velocity components, Figure 12(c). The contour level distribution changes compared to the more upstream chord-wise sections displayed in Figure 12(a) and Figure 12(b).

In the vicinity of the inboard vortex, different levels of the normal velocity component indicate again the vortex axis. Especially for $x/c_r = 0.3$ and $x/c_r = 0.5$, the change in sign of the w_{mean}/U_∞ values is particularly seen, Figure 12(a) and Figure 12(b). More downstream, this effect is not as obvious, since the normal velocity component in the inboard wing section is overall dominated by negative w_{mean}/U_∞ values, Figure 12(c).

3.3 Turbulent Flow Field Characteristics

After the discussion of the mean velocity field, the turbulent kinetic energy k is considered. Together with the definition of the mean square values of the velocity fluctuations

$$u_{i,rms} = \sqrt{(u_i'^2)_{mean}}, \quad (1)$$

it is defined as a non-dimensional value to

$$k = \frac{u_{rms}^2 + v_{rms}^2 + w_{rms}^2}{2 \cdot U_\infty^2}. \quad (2)$$

In Figure 13, contour plots of the turbulent kinetic energy are presented at $\alpha = 16^\circ$ for three different chord-wise sections. For a better analysis, the contour levels are shown with a logarithmic scale. The inboard vortex structure can be observed very well, resulting in turbulent kinetic energy values in the range of $k \approx 0.01$. Moreover, the thickened boundary layer structure present in the more downstream region of the midboard wing sections is also noticed with comparable levels of k . The levels are up to two orders of magnitude larger than the surrounding freestream turbulent kinetic energy values.

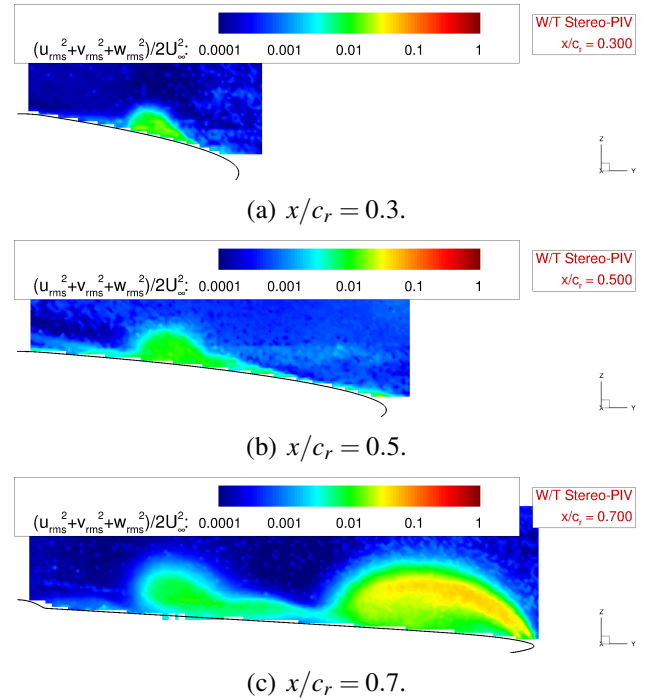


Fig. 13 Turbulent kinetic energy k for selected chord-wise sections at $\alpha = 16^\circ$.

Within the wing tip separation area, even higher values of the turbulent kinetic energy compared to those associated with the inboard vortex and the thickened boundary layer region are noticed, Figure 13(c). The maximum turbulent kinetic energy results in this chord-wise section in a value of $k \approx 0.06$. The highest values are found at the

separating shear layer and underneath within the recirculation area. The considerably increased levels of turbulent kinetic energy confirm thus the identification of the wing tip separation area as a region of irregular separated flow.

4 Conclusion and Outlook

Experimental investigations on the SAGITTA diamond wing W/T configuration have been presented and discussed in this article. For the angle of attack of $\alpha = 16^\circ$, the flow field has been analyzed in detail with respect to overall aerodynamic characteristics, mean velocity distributions and turbulent kinetic energy. The flow field investigations are based on W/T experiments applying Stereo Particle Image Velocimetry (Stereo PIV). It turns out that the measurement setup is well suited for the present diamond wing application. Reasonable flow field characteristics are obtained down to the W/T model surface, which have been analyzed in this paper for selected chord-wise sections.

Two main flow phenomena dominate the flow field characteristics of the SAGITTA diamond wing configuration with increasing angle of attack. On the one hand, the sharp inboard leading-edge contour provokes an inboard leading-edge vortex that deviates from the leading-edge, when the leading-edge contour changes to rounded type. The inboard vortex aligns then to the main flow direction and moves downstream over the inboard section of the diamond wing surface. On the other hand, a region of separated flow with flow reversal is formed at the diamond wing tip. This flow structure is not of common vortex type, but results in an area of irregular separated flow. In between of the two structures of separated flow, attached flow is present at the rounded leading-edge contour. In the more downstream region of the midboard wing sections, however, the attached flow is further influenced by the two dominating flow separations, and the boundary layer is thickened. With increasing angle of attack, this results in a separation bubble with irregular flow.

With the conducted W/T experiments, a valuable data base has been set up for the SAGITTA

diamond wing W/T configuration. Thereby, numerical results such as the one already published in [3] can be validated by the experimental data sets. In particular, the sectional contour plots presented in this article can be compared to each other and analyzed more efficiently. In order to enlarge the experimental data base even more, Stereo PIV measurements at asymmetric freestream conditions are of high interest. With regard to stability and control concerns of the SAGITTA diamond wing configuration at more complex flight attitudes (angle of attack and sideslip angle combinations), the detailed understanding of the occurring flow phenomena is required. Therefore, exact knowledge of the flow field gained from additional Stereo PIV measurements would be of high value.

5 Acknowledgements

The authors gratefully acknowledge Airbus Defence & Space for the support of this investigation within the SAGITTA research program. Moreover, the support of our colleague Moritz Grawunder in helping with all Stereo PIV questions and the work of our student Andrei Buzica is highly appreciated.

References

- [1] Gursul, I., Gordnier, R., and Visbal, M., "Unsteady Aerodynamics of Non-Slender Delta Wings," *Progress in Aerospace Sciences*, Vol. 41, No. 1, 2005, pp. 515–557.
- [2] Luckring, J. M., "A Survey of Factors Affecting Blunt Leading-Edge Separation for Swept and Semi-Slender Wings," *28th AIAA Applied Aerodynamics Conference, Chicago, United States, June 28 – July 01, 2010*, No. 4820 in AIAA 2010.
- [3] Hövelmann, A. and Breitsamter, C., "Leading-Edge Geometry Effects on the Vortex System Formation of a Diamond Wing Configuration," *31st AIAA Applied Aerodynamics Conference, San Diego, United States, June 24–27, 2013*, No. 3187 in AIAA 2013.
- [4] Schütte, A., Hummel, D., and Hitzel, S. M., "Flow Physics Analyses of a Generic Unmanned Combat Aerial Vehicle Configuration,"

Journal of Aircraft, Vol. 49, No. 6, 2012, pp. 1638–1651.

- [5] Seifert, J., “SAGITTA - Nationale Forschungs-kooperation für fortschrittliche UAV-Technologien im Rahmen der Open Innovation Initiative von Cassidian,” *61th Deutscher Luft- und Raumfahrtkongress, Berlin, Germany, September 10–12, 2012*, No. 1352 in DGLR 2012.
- [6] Hövelmann, A. and Breitsamter, C., “Aerodynamic Characteristics of the SAGITTA Diamond Wing Demonstrator Configuration,” *61th Deutscher Luft- und Raumfahrtkongress, Berlin, Germany, September 10–12, 2012*, No. 1220 in DGLR 2012.
- [7] Breitsamter, C., “Aerodynamic Efficiency of High Maneuverable Aircraft Applying Adaptive Wing Trailing Edge Section,” *24th International Congress of the Aeronautical Sciences, Yokohama, Japan, August 29 – September 3, 2004*, No. 4.3.2 in ICAS 2004.
- [8] Raffel, M., Willert, C. E., Wereley, S., and Kompenhans, J., *Particle Image Velocimetry – A Practical Guide*, 2nd Edition, Springer Verlag, ISBN 978-3-540-72307-3, 2007.
- [9] Furman, A. and Breitsamter, C., “Stereo-PIV and Hot-Wire Investigations on Delta Wing With Sharp and Rounded Leading Edge,” *1st CEAS European Air and Space Conference, Berlin, Germany, September 10 –13, 2007*, No. 430 in CEAS 2007.
- [10] Konrath, R., Klein, C., Schröder, A., and Kompenhans, J., “Combined Application of Pressure Sensitive Paint and Particle Image Velocimetry to the Flow Above a Delta Wing,” *Experiments in Fluids*, Vol. 44, No. 3, 2008, pp. 357–366.
- [11] Roosenboom, E. W. M., Konrath, R., Schröder, A., Pallek, D., and Otter, D., “Stereoscopic Particle Image Velocimetry Flowfield Investigation of an Unmanned Combat Air Vehicle,” *Journal of Aircraft*, Vol. 49, No. 6, 2012, pp. 1584–1596.
- [12] Furman, A. and Breitsamter, C., “Turbulent and Unsteady Flow Characteristics of Delta Wing Vortex Systems,” *Aerospace Science and Technology*, Vol. 24, No. 1, 2013, pp. 32–44.
- [13] Breitsamter, C., *Turbulente Strömungsstrukturen an Flugzeugkonfigurationen mit Vorderkantenwirbeln*, Dissertation, Technische Universität München, Herbert Utz Verlag, ISBN 3-89675-201-4, 1997.

Copyright Statement

The authors confirm that they, and/or their company or organization, hold copyright on all of the original material included in this paper. The authors also confirm that they have obtained permission, from the copyright holder of any third party material included in this paper, to publish it as part of their paper. The authors confirm that they give permission, or have obtained permission from the copyright holder of this paper, for the publication and distribution of this paper as part of the ICAS 2014 proceedings or as individual off-prints from the proceedings.